Torque Density Improvement of a Low-Speed High-Torque Swirling Actuator Driven by Electromagnetic Radial Force With Integrated Mechanical Gears

LINGYU CHEN (Student Member, IEEE), **YUSUKE FUJII** (Member, IEEE),
AND AKIRA CHIBA (Fellow, IEEE)

Department of Electrical and Electronic Engineering, Tokyo Institute of Technology, Tokyo 152-8550, Japan

CORRESPONDING AUTHOR: LINGYU CHEN (email: chen.l@belm.ee.titech.ac.jp)

ABSTRACT The torque density improvement of a low-speed high-torque swirling actuator is presented in this article. The swirling actuator is driven by the electromagnetic radial force and integrated mechanical gears. The electromagnetic radial force generates the circular motion of the swirler, which is converted into the low-speed rotor rotation by the mechanical gears. First, the dimensions of the swirler with 12-pole permanent magnets are optimized to enhance the electromagnetic radial force by analytical calculation and three-dimensional finite-element analysis. Second, an improved gear set with a reduced pressure angle and an increased transmission ratio is designed. The gear efficiency and torque are investigated analytically considering the friction loss. Two prototypes are designed, and the experimental results exhibit that the peak torque density is improved from 27 to 64 Nm/L with a small volume of 0.16 L.

INDEX TERMS Electromagnetic radial force, low-speed high-torque machines, mechanical gears, swirling actuators.

I. INTRODUCTION

Low-speed high-torque electric machines are widely utilized in applications, such as wind turbines [1], traction motors [2], and industrial robots [3]. There are two main categories of low-speed high-torque electric machines. The first is the geared machine, which combines the high-speed electric machine and speed reducer. The second is the direct-drive electric machine.

Geared machines can achieve high-torque densities with high-transmission-ratio speed reducers. Typical mechanical speed reducers include spur gears, planetary gears, cycloidal drives, and strain wave gears. In [4], a bilateral-drive planetary gear with a high transmission ratio of up to 96.2 was proposed for robotic actuators. The two-stage speed reducer that combines the planetary gear and cycloidal drive can reach a transmission ratio of up to 204 [5]. The strain wave gear has a high single-stage transmission ratio with a compact size. For example, the actuators FHA-mini equipped with strain wave

gears have peak torque densities of 36–63 Nm/L when the transmission ratio is 50, whereas the peak torque densities increase to 52–99 Nm/L when the transmission ratio is 100 [6].

Compared with geared machines, direct-drive electric machines need less regular maintenance. Moreover, the no-backlash characteristic makes them suitable for precise position control. For conventional permanent magnet (PM) machines, a large pole number is necessary to realize low speed and high torque. The 22-pole direct-drive PM motors in [7] and [8] have the peak torque densities of 7 and 17 Nm/L with the identical volume of 0.13 L, whereas the 40-pole direct-drive PM motor in [9] has a peak torque density of 21 Nm/L with a volume of 0.15 L. There have been some notable direct-drive machines aiming to improve the torque density. In [10], a claw-pole-stator PM motor was proposed. The stator has 3 claw-pole layers and the rotor has 20 poles of PMs. A peak torque density of 37.7 Nm/L was realized with

a volume of 0.2 L in three-dimensional (3-D) finite-element analysis (FEA). In [11], an outer-rotor switched flux memory machine was presented. The hybrid stator has low-coercive-force magnets and rare-earth PMs, both of which are in the spoke-type configuration. The optimized model reached a continuous torque density of 31.6 Nm/L with a volume of 0.16 L in 3-D FEA. In [12], a double-stator spoke-array PM vernier machine realized a continuous torque density of 66 Nm/L with a large volume of 30 L. In [13], a combined radial-axial flux PM vernier machine was developed. A set of toroidal windings were configured on the stator and the end-windings were utilized to couple with the axial rotors. With the enlarged rotor area that contributes to torque generation, the torque density was enhanced to 58 Nm/L in a 34-pole model with a volume of 5.4 L.

Magnetic gears utilize the flux modulation effect to realize noncontact speed reduction and power transmission [14]. Among magnetic gears, coaxial magnetic gears normally have low transmission ratios, whereas cycloidal magnetic gears can have higher transmission ratios [15]. Many magnetic-geared machines integrating the coaxial magnetic gears have been reported. In [16], the coaxial magnetic gear was connected to a PM machine in the axial direction. In [17], an outer-rotor PM motor was inserted inside the high-speed rotor of a coaxial magnetic gear to build a magnetic-geared motor. The torque density was 40 Nm/L with a volume of 3.5 L. In [18], a stator with nonoverlapping windings was combined with the outer rotor of the coaxial magnetic gear. The resultant machine is known as the pseudo direct drive. A continuous torque density of over 60 Nm/L with a volume of 1.9 L was reported. The magnetic-geared machine in [19] has an inner stator, a modulation ring, and an outer rotor. Both the modulation ring and outer rotor have consequent-pole PMs. Thus, the machine was named as the dual-layer magnetic-geared PM machine. The peak torque density reached 89 Nm/L with a volume of 5.7 L in FEA. In addition, Halbach-layer PMs were adopted in the dual-layer magnetic-geared PM machine in [20]. The authors realized the torque density of 77.3 Nm/L with a volume of 4.9 L at the current density of 8 A/mm^2 and stated that the torque density could exceed 150 Nm/L with a higher current density. In [21], an axial-flux focusing magnetic gear was integrated with an outer stator for an ocean generator application. The machine volume was 5 L and the calculated and measured peak torque densities were 114 and 94.4 Nm/L, respectively.

The proposed swirling actuator is driven by the electromagnetic radial force, which leads to the circular motion of the swirler [22]. The identical motion can be found in several special cycloidal motors. In [23], the cyclic expansion and contraction of the shape-memory-alloy wires generate the circular motion. In [24], the external rotating magnetic fields generate the circular motion. Involute-type mechanical gears were integrated in [22], [23], and [24] to convert the circular motion into low-speed rotation. The gear mechanism is identical to that of cycloidal drives. A high transmission ratio can be achieved by a small gear tooth number difference.

FIGURE 1. Basic structure of the swirling actuator.

The principle of the proposed swirling actuator was verified in our previous article [22]; however, we could only achieve a peak torque density of 27 Nm/L with a small volume of 0.16 L. In contrast, the direct-drive PM machines with similar volumes of 0.1–0.2 L have the peak torque densities up to 37.7 Nm/L [7], [8], [9], [10], [11]. In this article, the peak torque density of the swirling actuator is improved to 64 Nm/L with the identical volume of 0.16 L. The target applications of the swirling actuator are robotic joints and wearable rehabilitation devices, which operate at very low speeds and require high-torque densities with compact sizes. Conventional geared machines have electric motors and mechanical gears connected in the axial direction, whereas the swirling actuator integrates the electromagnetic part and mechanical gears in the radial direction. The flat structure of the swirling actuator is attractive for applications, such as the wearable exoskeleton [25].

Section II introduces the basic structure and operation principle of the swirling actuator. In Section III, the electromagnetic radial force is enhanced by the optimization of swirler dimensions. Section IV investigates the design of mechanical gears. Experimental results of two prototypes are presented in Section V to evaluate the torque density improvement. Section VI provides the conclusions.

II. BASIC STRUCTURE AND OPERATION PRINCIPLE

Fig. 1 shows the basic structure of the swirling actuator. Three-phase double-layer nonoverlapping windings are wound around the teeth of the inner stator. The swirler surrounds the stator and has 12-pole PMs mounted on the inner surface. The swirler has a circular motion with a nominal radius of r_0 and an angular speed of ω_s. The pins through the swirler holes prevent the rotation and allow only the radial movement of the swirler. There are Z_{sw} gear teeth on the

outer surface of the swirler and Z_r gear teeth on the inner surface of the rotor. The gears convert the circular motion of the swirler into the rotor rotation at an angular speed of ω_r. The transmission ratio G between ω_s and ω_r is given by the gear tooth numbers as

$$G = \frac{\omega_s}{\omega_r} = \frac{Z_r}{Z_r - Z_{\mathrm{sw}}}. \tag{1}$$

The electromagnetic radial force is generated between the stator and swirler. Let us define p_s and p_{sw} as the pole-pair numbers of the magnetomotive forces (MMFs) generated by the stator windings and swirler PMs, respectively. Based on the principle of bearingless motors [26], to generate the active radial force, p_s and p_{sw} should satisfy the following equation:

$$p_s = p_{\mathrm{sw}} \pm 1. \tag{2}$$

The 12-pole PMs on the swirler mainly generate the six pole-pair MMF. Thus, the stator windings in Fig. 1 are designed to generate the five and seven pole-pair MMFs.

The resultant electromagnetic radial force can be decomposed into F_d and F_q. The F_d is in the eccentric direction of the swirler and F_q is perpendicular to F_d. In Fig. 1, the swirler is eccentric in the x-direction. Thus, the d- and q-axes are on the x- and y-axes, respectively. The swirler has the velocity $\boldsymbol{v_{sw0}}$ in the q-axis with the magnitude of $\omega_s r_0$. Thus, the mechanical power P_{sw0} of the swirler is given by

$$P_{\mathrm{sw0}} = F_q v_{\mathrm{sw0}} = F_q \omega_s r_0. \tag{3}$$

The mechanical power of the rotor is given by

$$P_r = \omega_r T \tag{4}$$

where T is the rotor output torque. The gear efficiency η_g is defined as

$$\eta_g = \frac{P_r}{P_{\mathrm{sw0}}}. \tag{5}$$

By substituting (1), (3), and (5) into (4), the rotor output torque is derived as

$$T = F_q r_0 G \eta_g. \tag{6}$$

Equation (6) indicates that the rotor output torque can be enhanced by increasing the electromagnetic radial force F_q, transmission ratio G, and gear efficiency η_g. The nominal swirler eccentric radius r_0 should be equal to the nominal center distance between the rotor and swirler gears. The calculation of the gear center distance is introduced in the Appendix. In our previous article [22], the nominal gear center distance was 0.5 mm. Thus, r_0 is also set as 0.5 mm in this article. Note that r_0 should be shorter than the nominal air-gap length g_0, which is the air-gap length when the swirler is concentric with the stator.

III. ENHANCEMENT OF ELECTROMAGNETIC RADIAL FORCE

Fig. 2 shows the waveforms for the analytical calculation of the air-gap radial flux density. The horizontal axis is the
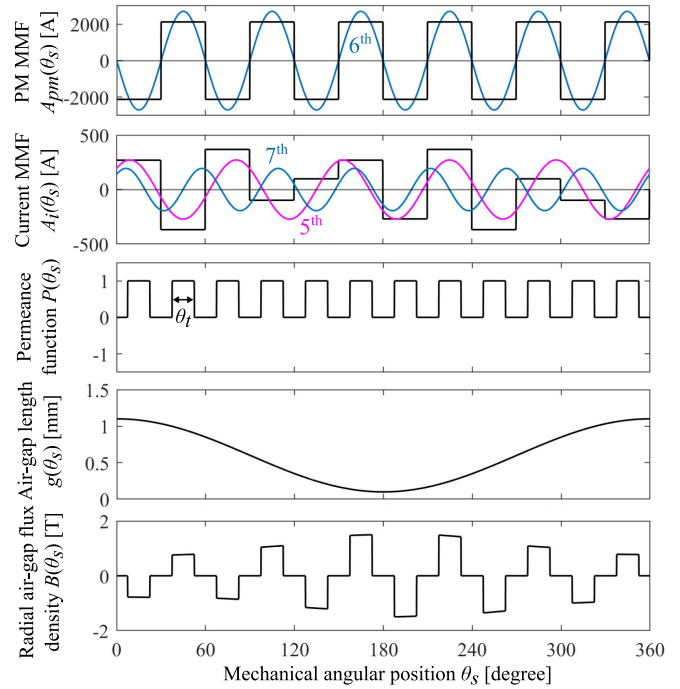
FIGURE 2. Waveforms for analytical calculation of the radial air-gap flux density.

mechanical angular position θ_s in the static coordinate system. The $A_{\mathrm{pm}}(\theta_s)$ and $A_i(\theta_s)$ are the MMFs generated by the swirler PMs and stator currents, respectively. For $k = 1, 2, 3, \ldots$, the 12-pole PMs generate $[(2k-1)6]$th MMF components, whereas the 12-slot double-layer nonoverlapping windings can generate $[(2k-1)6 \pm 1]$th MMF components to satisfy (2) for active radial force generation. In Fig. 2, the dominant sixth component of $A_{\mathrm{pm}}(\theta_s)$ and fifth and seventh components of $A_i(\theta_s)$ are shown. The $P(\theta_s)$ is the permeance function describing the stator slot effect and θ_t is the span angle of the stator teeth. The $g(\theta_s)$ is the nonuniform air-gap length between the stator and swirler. Let us define θ_d as the swirler eccentric direction angle and set the initial value of θ_d as 0. Then, θ_d is given by

$$\theta_d = \omega_s t. \tag{7}$$

Using θ_d, $g(\theta_s)$ is derived as

$$g(\theta_s) \approx g_0 + r_0 \cos(\theta_s - \theta_d). \tag{8}$$

The radial air-gap flux density $B(\theta_s)$ is given as

$$B(\theta_s) = \frac{\mu_0 [A_{\mathrm{pm}}(\theta_s) + A_i(\theta_s)] P(\theta_s)}{g(\theta_s) + t_m/\mu_r} \tag{9}$$

where μ_0 is the permeability of vacuum; and μ_r and t_m are the relative permeability and thickness of PMs, respectively. As shown in Fig. 2, the amplitude of $B(\theta_s)$ is high where the air-gap length is short.

Using Maxwell's stress tensor method [27] and considering only the radial air-gap flux density [28], the electromagnetic

radial forces on the swirler in the static coordinate system are derived as

$$F_x = -\frac{r_s l_s}{2\mu_0} \int_{-\pi}^{\pi} [B(\theta_s)]^2 \cos\theta_s d\theta_s \qquad (10)$$

$$F_y = -\frac{r_s l_s}{2\mu_0} \int_{-\pi}^{\pi} [B(\theta_s)]^2 \sin\theta_s d\theta_s \qquad (11)$$

where r_s is the stator outer radius and l_s is the stack length. Using θ_d, F_x and F_y are transformed into the rotational dq coordinate system as

$$\begin{bmatrix} F_d \\ F_q \end{bmatrix} = \begin{bmatrix} \cos\theta_d & \sin\theta_d \\ -\sin\theta_d & \cos\theta_d \end{bmatrix} \begin{bmatrix} F_x \\ F_y \end{bmatrix}. \qquad (12)$$

The stator phase currents i_u, i_v, and i_w are also transformed into the d- and q-axis currents as

$$\begin{bmatrix} i_d \\ i_q \end{bmatrix} = \sqrt{\frac{2}{3}} \begin{bmatrix} \cos\theta_d & \sin\theta_d \\ -\sin\theta_d & \cos\theta_d \end{bmatrix} \begin{bmatrix} 1 & -\frac{1}{2} & -\frac{1}{2} \\ 0 & \frac{\sqrt{3}}{2} & -\frac{\sqrt{3}}{2} \end{bmatrix} \begin{bmatrix} i_u \\ i_v \\ i_w \end{bmatrix}. \qquad (13)$$

Note that the d-axis in a conventional PM motor is based on the rotational angular position of the rotor PMs, whereas the d-axis in the swirling actuator is based on the swirler eccentric direction.

To simplify the analytical derivations of F_d and F_q, only the dominant sixth component of $A_{\text{pm}}(\theta_s)$ and the fifth and seventh components of $A_i(\theta_s)$ are considered. Thus, $A_{\text{pm}}(\theta_s)$ is given as

$$A_{\text{pm}}(\theta_s) \approx -\frac{4B_r t_m}{\pi\mu_0\mu_r} \sin 6\theta_s \qquad (14)$$

where B_r is the residual flux density of PMs. The $A_i(\theta_s)$ is given as

$$A_i(\theta_s) \approx A_{I5} \sin(5\theta_s + \omega_s t + \theta_i)$$
$$+ A_{I7} \sin(7\theta_s - \omega_s t - \theta_i) \qquad (15)$$

where θ_i is the initial phase shift of the phase currents. The amplitudes A_{I5} and A_{I7} are derived as

$$A_{I5} = \frac{12}{5\pi}\cos^2\left(\frac{\pi}{12}\right)N_s I_s, \quad A_{I7} = \frac{12}{7\pi}\cos^2\left(\frac{\pi}{12}\right)N_s I_s \qquad (16)$$

where N_S is the turn number per stator tooth and I_s is the amplitude of the phase currents. Moreover, the following approximation is conducted:

$$\frac{1}{g(\theta_s) + t_m/\mu_r} \approx \frac{1}{g_0 + t_m/\mu_r} - \frac{r_0 \cos(\theta_s - \theta_d)}{(g_0 + t_m/\mu_r)^2}. \qquad (17)$$

From (7) to (17), F_d and F_q are simplified into

$$\begin{bmatrix} F_d \\ F_q \end{bmatrix} = k_d \begin{bmatrix} r_0 \\ 0 \end{bmatrix} + k_i \begin{bmatrix} i_d \\ i_q \end{bmatrix} \qquad (18)$$

where k_d and k_i are the displacement force factor and current force factor, respectively. The k_d and k_i are derived as

$$k_d = \frac{8r_s l_s (\sin 3\theta_t)^2 B_r^2 t_m^2}{\pi\mu_0\mu_r^2(g_0 + t_m/\mu_r)^3} \qquad (19)$$
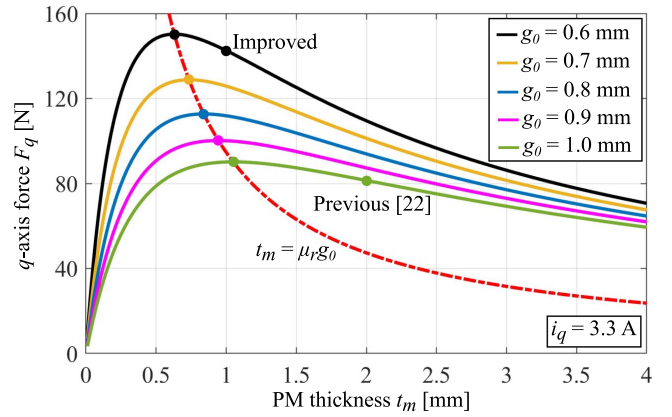
FIGURE 3. Analytical results of the q-axis force F_q with respect to the nominal air-gap length g_0 and PM thickness t_m.

$$k_i = \left(\frac{1}{5}\sin\frac{5\theta_t}{2} + \frac{1}{7}\sin\frac{7\theta_t}{2}\right)\frac{8\sqrt{6}N_s r_s l_s \sin 3\theta_t \cos\frac{\pi}{12}B_r t_m}{\pi\mu_r^2(g_0 + t_m/\mu_r)^2}. \qquad (20)$$

The partial derivative of k_i with respect to t_m is derived as

$$\frac{\partial k_i}{\partial t_m} = \left(\frac{1}{5}\sin\frac{5\theta_t}{2} + \frac{1}{7}\sin\frac{7\theta_t}{2}\right)\frac{8\sqrt{6}N_s r_s l_s B_r \sin 3\theta_t \cos\frac{\pi}{12}}{\pi\mu_r^2}$$
$$\times \frac{g_0 - t_m/\mu_r}{(g_0 + t_m/\mu_r)^3}. \qquad (21)$$

For a certain value of g_0, k_i reaches the maximum when (21) is zero, i.e., the PM thickness $t_m = \mu_r g_0$.

Fig. 3 shows the analytical results of F_q with respect to t_m. The i_d is zero and i_q is 3.3 A. There are five solid curves corresponding to different values of g_0 from 0.6 to 1.0 mm with a step of 0.1 mm. Moreover, the red dashed curve satisfying $t_m = \mu_r g_0$ is also shown, which intersects with the other five curves at the peak points. The F_q increases as g_0 becomes short. Thus, the design point should be on the curve satisfying $t_m = \mu_r g_0$, and has a g_0 as short as possible. As the relative permeability of PMs μ_r is close to 1, the PMs are expected to be as thin as the air-gap length. However, in the real design, PMs thinner than 1 mm are avoided due to the fabrication difficulty and possible irreversible demagnetization. In [22], the design point was at $t_m = 2$ mm and $g_0 = 1$ mm. In this article, $g_0 = 0.6$ mm and $t_m = 1$ mm are selected.

The optimization is verified by 3-D FEA. Fig. 4 shows the FEA and calculated results of electromagnetic radial forces F_d and F_q with respect to the q-axis current i_q. The calculated forces are obtained by numerical integrations using the original waveforms of $A_{\text{pm}}(\theta_s)$, $A_i(\theta_s)$, and $g(\theta_s)$. The d-axis current i_d is zero. The F_d does not change with i_q, whereas F_q is proportional to i_q. The calculated results agree well with the FEA results. The current force factor k_i is enhanced from 27.5 to 51.2 N/A in the improved electromagnetic part. The F_d when $i_d = 0$ is also enhanced from 94 to 173 N.
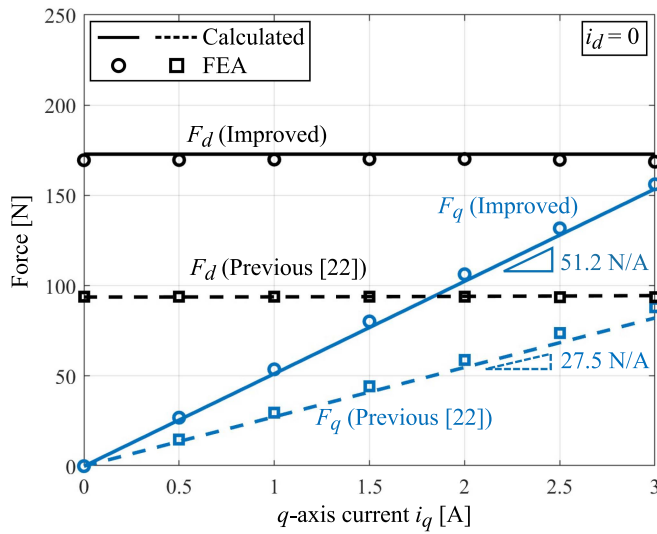
FIGURE 4. FEA and calculated results of radial force components with respect to the *q*-axis current i_q.

IV. GEAR DESIGN INVESTIGATION

In our previous article [22], it was indicated that the gear design parameters may affect the actual eccentric radius of the swirler and gear efficiency. Moreover, (6) shows that increasing the transmission ratio is expected to enhance the output torque. In this section, the gear design parameters are investigated, and a new gear set with identical dimensions and a higher transmission ratio is designed. The gear efficiency is analyzed and the effects of gear design parameters on the output torque are illustrated.

A. GEAR DESIGN PARAMETERS

Fig. 5 shows two gear sets to explain the effect of the pressure angle. The swirler gear is eccentric and meshes with the rotor gear in the *x*-direction. At the meshing point, there is a pressure force F_{sw} on the swirler perpendicular to the tooth surface. The F_{sw} can be decomposed into the radial force F_r and tangential force F_t. The angle between F_t and F_{sw} is the pressure angle α. The F_{sw} and F_t can be written as the functions of F_r

$$F_{sw} = \frac{F_r}{\sin \alpha} \tag{22}$$

$$F_t = \frac{F_r}{\tan \alpha}. \tag{23}$$

The tangential force F_t generates the rotor output torque. If the friction is ignored, the rotor output torque is given by

$$T = F_t r_r \tag{24}$$

where r_r is the rotor pitch circle radius. By substituting (23) into (24), the rotor output torque is given by

$$T = \frac{F_r r_r}{\tan \alpha}. \tag{25}$$
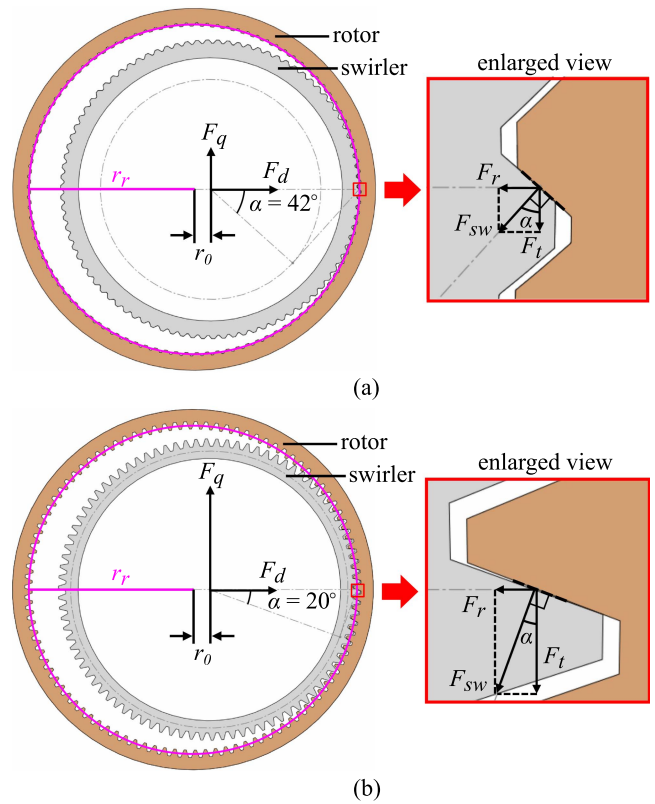
FIGURE 5. Gear sets with different pressure angles α. (a) $\alpha = 42°$. (b) $\alpha = 20°$.
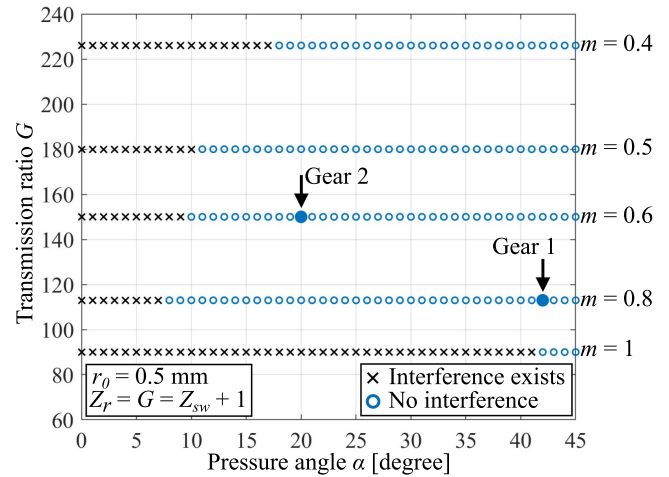
FIGURE 6. Gear design candidates.

The gear set in Fig. 5(a) has a large pressure angle α of 42°, which is identical to the previous prototype in [22]. In contrast, the gear set in Fig. 5(b) has a smaller α of 20°. From (25), with the identical F_r, the gear set in Fig. 5(b) can generate a higher torque because of the smaller α.

Fig. 6 shows the gear design candidates. The rotor tooth number is given by

$$Z_r = \frac{2r_r}{m} \tag{26}$$
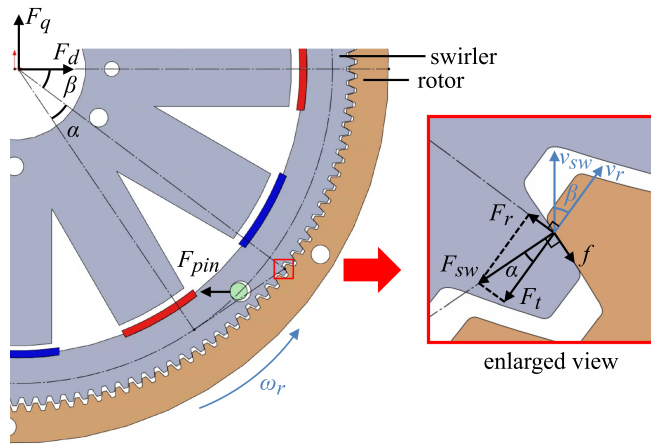
FIGURE 7. Forces on the swirler and velocities of the swirler and rotor.

FIGURE 8. Calculated torque with respect to the transmission ratio **G**.

where m is the module describing the size of gear teeth. The values of m in Fig. 6 are 0.4, 0.5, 0.6, 0.8, and 1 mm, which are standard values listed in JISB1702-1. As m decreases, the gear tooth becomes smaller and the tooth numbers increase. The rotor pitch circle radius r_r is about 45 mm and should lead to integer tooth numbers. The tooth number difference $(Z_r - Z_{sw})$ is set as 1 to maximize the transmission ratio G according to (1). For involute-type gears, such a small tooth number difference may cause undesirable tooth interference. The method to check the interference is introduced in Chapter 2.9 of [29]. The selected gears should have no interference. Gear 1 with $\alpha = 42°$ and $G = 113$ was used in the previous prototype in [22]. According to (6) and (25), a small α and a large G are desirable to enhance the output torque. Thus, in the prototypes in this article, Gear 2 with $\alpha = 20°$ and $G = 150$ is adopted.

B. ANALYSIS OF GEAR EFFICIENCY

Fig. 7 shows the forces on the swirler and the velocities of the swirler and rotor. The F_{pin} is the pressure force from the pins. The friction f on the tooth surface is perpendicular to F_{sw}. Let us define the actual eccentric radius of the swirler as r_m. It will be shown in Section V that r_m is shorter than the nominal eccentric radius r_0 and depends on the operation points. The β is the angle between the swirler eccentric direction and meshing angular position. From (47) in the Appendix, β is derived as

$$\beta = \arccos\left[\frac{(Z_r - Z_{\mathrm{sw}})m}{2r_m}\cos\alpha\right] - \alpha. \tag{27}$$

When the actuator is in the steady state, the resultant force of the swirler is the centripetal force towards the stator center. The forces on the swirler in the radial and tangential directions satisfy the following equations:

$$F_r + (F_{\mathrm{pin}} - F_d)\cos\beta + F_q\sin\beta - f\cos\alpha = m_{\mathrm{sw}}\omega_s^2 r_m\cos\beta \tag{28}$$

$$F_t + (F_{\mathrm{pin}} - F_d)\sin\beta - F_q\cos\beta + f\sin\alpha = m_{\mathrm{sw}}\omega_s^2 r_m\sin\beta \tag{29}$$

where m_{sw} is the swirler mass. The friction f is given by

$$f = \mu F_{\mathrm{sw}} \tag{30}$$

where μ is the coefficient of friction. The swirler velocity $\boldsymbol{v_{sw}}$ is in the q-axis, whereas the rotor velocity $\boldsymbol{v_r}$ at the meshing point is in the tangential direction. The angle between $\boldsymbol{v_{sw}}$ and $\boldsymbol{v_r}$ is β. When β is not zero, there is a relative motion between the swirler and rotor at the meshing point. The friction loss P_f is calculated as

$$P_f = (f\cos\alpha)(v_{\mathrm{sw}}\sin\beta) + (f\sin\alpha)(v_{\mathrm{sw}}\cos\beta - v_r). \tag{31}$$

The magnitudes of the velocities are

$$v_{\mathrm{sw}} = \omega_s r_m, \; v_r = \omega_r r_r \tag{32}$$

Then, the mechanical power of the rotor considering the friction loss is given by

$$P_r = F_q v_{\mathrm{sw}} - P_f = F_q\omega_s r_m - P_f. \tag{33}$$

By substituting (3) and (33) into (5), the gear efficiency η_g is given by

$$\eta_g = \frac{F_q\omega_s r_m - P_f}{F_q\omega_s r_0}. \tag{34}$$

Finally, by (1), (6), (22), (23), and (28)–(34), the rotor output torque is derived as

$$T = F_q G\left[r_m\cos(a+\beta) + \frac{\mu r_r\sin\alpha}{G}\right]$$
$$\times\left[\frac{1}{\mu\sin(a+\beta) + \cos(a+\beta)}\right]. \tag{35}$$

Fig. 8 shows the calculated torque with respect to G. The eccentric radius r_m, q-axis force F_q, and pressure angle α are set as 0.5 mm, 100 N, and 20°, respectively. The coefficient of friction μ depends on the gear materials, lubrication, fabrication accuracy, and surface roughness. It is difficult to calculate or measure μ at this stage. Here, μ is assumed to be 0.3, 0.4, and 0.5. Fig. 8 indicates that the torque increases
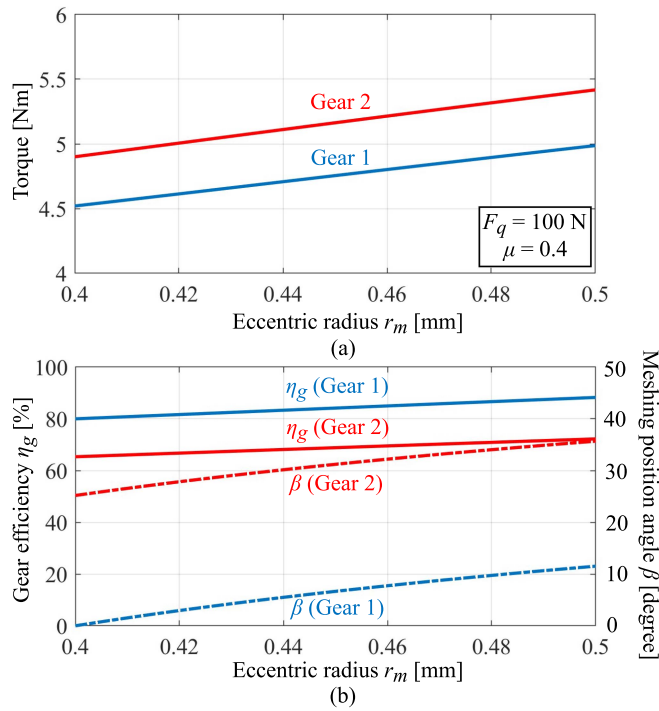
FIGURE 9. (a) Calculated torques with respect to r_m. (b) Calculated gear efficiencies η_g and meshing position angle β with respect to r_m.

TABLE 1. Specifications of Prototypes

	Previous [22]	Prototype 1	Prototype 2
Outer diameter [mm]		100	
Axial length with coil-ends [mm]		20	
Nominal eccentric radius r_0 [mm]		0.5	
Nominal air-gap length g_0 [mm]	1	0.6	0.6
PM thickness t_m [mm]	2	1	1
Rotor pitch circle radius r_r [mm]	45.2	45.2	45
Module m	0.8	0.8	0.6
Pressure angle α [°]	42	42	20
Transmission ratio G	113	113	150
Swirler gear material	440C	1045	1045
Rotor gear material	304	304	304
Rated/maximum speed [r/min]	5/30	5/30	5/30
Rated/peak torque [Nm]	1.3/4.2	3.6/7.4	4.1/10.0
Peak torque density [Nm/L]	27	47	64
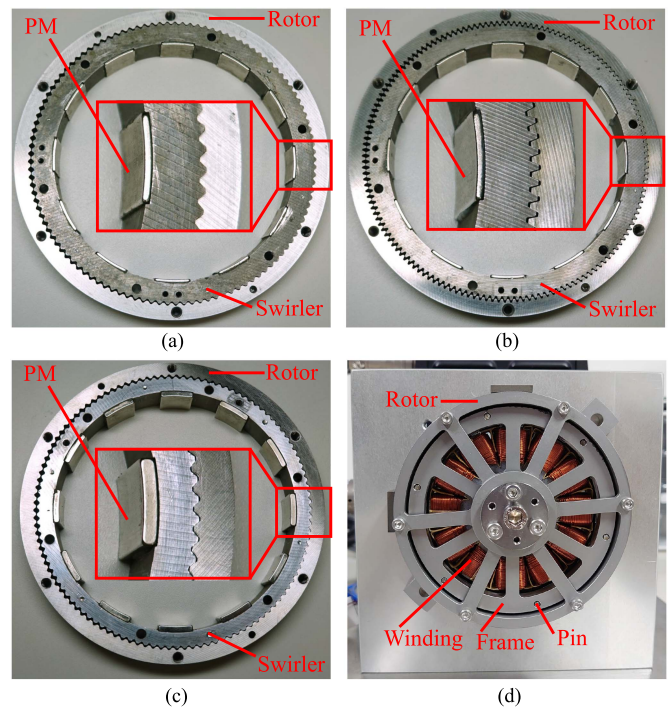
FIGURE 10. Pictures of fabricated gears of (a) prototype 1; (b) prototype 2; and (c) previous prototype in [22]. (d) Picture of the complete prototype.

as G increases, but on the other hand, it decreases when μ increases. Gear 2 increases the transmission ratio from 113 to 150 compared with Gear 1. This time, even higher transmission ratios are not attempted because the small gear teeth may have a problem in mechanical fabrication precision.

Fig. 9(a) shows the calculated torques of Gear 1 and Gear 2 with respect to r_m when $F_q = 100$ N and $\mu = 0.4$. Fig. 9(b) shows the calculated η_g and β with respect to r_m of Gear 1 and Gear 2. It is observed that the gear efficiency η_g increases as the eccentric radius r_m increases. The reason is that the rotor mechanical power P_r increases as r_m increases as shown in (34). Moreover, the maximum efficiency of Gear 2 is 72%, whereas the maximum efficiency of Gear 1 is 88%. As shown in Fig. 7, a large β indicates that the relative velocity between the swirler and rotor is high. As a result, the friction loss P_f is high. The gear efficiency of Gear 2 is lower than that of Gear 1 due to the larger β of Gear 2. However, Gear 2 has a higher torque than Gear 1 owing to the high transmission ratio.

V. EXPERIMENTS

Two prototypes were built to verify the torque density improvement by 1) the electromagnetic optimization and 2) the improved gear design. Table 1 lists the specifications of Prototype 1, Prototype 2, and the previous prototype in [22]. Compared with the previous prototype, Prototype 1 reduces the nominal air-gap length and PM thickness to enhance the electromagnetic radial force. Prototype 2 further adopts the new Gear 2 with a reduced pressure angle and an enlarged transmission ratio. Fig. 10(a)–(c) shows the fabricated gears

of Prototype 1, Prototype 2, and the previous prototype in [22]. Fig. 10(d) shows the complete prototype including the mechanical structure.

A. MECHANICAL DESIGN OF PROTOTYPES

Fig. 11 shows the front sectional view of the 3-D model of the prototypes. The pins go through the frames and swirler to prevent the rotation and restrict the eccentric radius of the swirler. The shaft is fixed with the rotor gear and supported by two mechanical bearings. As shown in Fig. 7, the unbalanced radial force on the rotor is

$$F_{ur} = F_r - f \cos \alpha. \qquad (36)$$
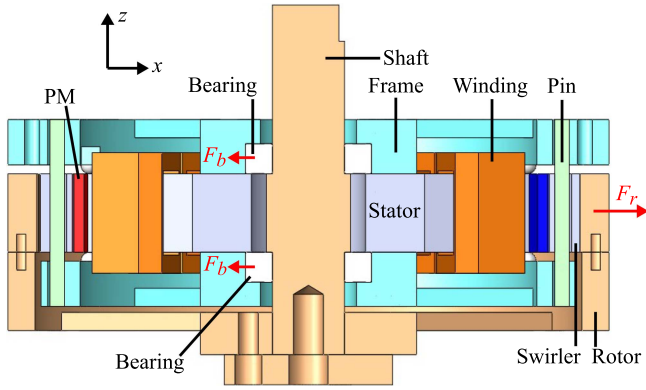
FIGURE 11. Front sectional view of the prototypes.
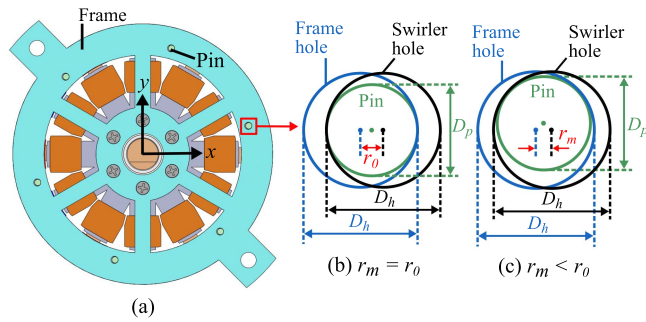
FIGURE 12. (a) Top view of the prototypes; (b) ideal pin configuration ($r_m = r_0$); and (c) actual pin configuration ($r_m < r_0$).

If the friction f is ignored, based on (25), F_{ur} is given by

$$F_{ur} = F_r = \frac{T \tan \alpha}{r_r}. \tag{37}$$

Equation (37) indicates that reducing the pressure angle α can reduce the unbalanced radial force F_{ur}. By changing α from 42° to 20°, F_{ur} is reduced by 60%. Moreover, the load force on a single bearing is given by

$$F_b = \frac{F_r}{2}. \tag{38}$$

The peak torque of prototype 2 is 10 Nm. From (37) and (38), the peak value of F_b is calculated to be 40 N, which is only 2% of the radial load capacity of 1920 N of the bearings (B6801ZZ). Thus, the unbalanced radial force has little effect on the lifetime of the bearings.

Fig. 12(a) shows the top view of the 3-D model of the prototypes including the six pins. Fig. 12(b) shows the ideal pin configuration when $r_m = r_0$. The diameters of frame holes and swirler holes are both D_h, whereas the diameter of the pins is D_p. The pins are tangential with the frame holes and swirler holes. The center distance between the frame holes and swirler holes is the eccentric radius of the swirler. To restrict the maximum eccentric radius to r_0, D_h and D_p need to satisfy

$$D_h - D_p = r_0. \tag{39}$$
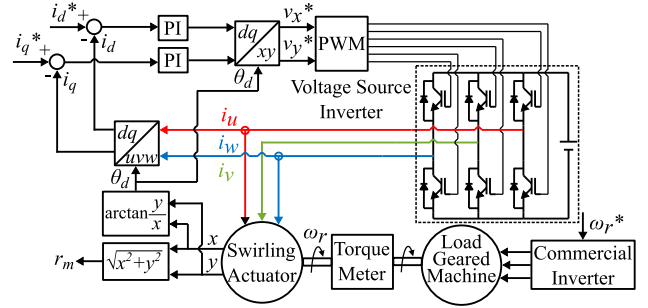
FIGURE 13. Control block diagram of the experimental setup of the swirling actuator.

In the prototypes, D_h and D_p are set as 2.8 and 2.3 mm, respectively. To prevent the rotation of the swirler, at least three pins are necessary. Moreover, the diameter of pins should be smaller than the width of the swirler gear. By increasing the number of pins to six, the load force on a single pin is reduced and thin pins can be used. The peak torque of prototype 2 was 10 Nm and the equivalent force that the pins need to overcome is 238 N. Considering the worst condition in which the force is applied on a single pin, the FEA result of the maximum von Mises stress on the pin is 185 MPa. In contrast, the yield strength of the pin material (stainless steel 440C) is 450 MPa. Thus, the pins have adequate stiffness.

In the actual operation, r_m is shorter than r_0 as shown in Fig. 12(c). It can be observed that the centers of the frame hole, swirler hole, and pin are no longer collinear when $r_m < r_0$. From Fig. 7, the force component imposed on the swirler tooth and opposite to F_d is given by

$$F_{dn} = F_r \cos \beta + F_t \sin \beta. \tag{40}$$

The swirler is pushed back towards the concentric position by F_{dn}. As a result, the eccentric radius r_m is reduced. By substituting (24) and (37) into (39), F_{dn} is derived as

$$F_{dn} = \frac{T}{r_r} (\tan \alpha \cos \beta + \sin \beta). \tag{41}$$

The F_{dn} increases as the torque increases. Consequently, the required F_d to overcome F_{dn} and keep r_m close to r_0 also increases.

B. TORQUE EVALUATION

Fig. 13 shows the control block of the swirling actuator. A three-phase voltage source inverter drives the swirling actuator. Two displacement sensors measure the displacements x and y of the swirler in the x- and y-directions. The eccentric direction angle θ_d and eccentric radius r_m are given by

$$\theta_d = \arctan \frac{y}{x}, \quad r_m = \sqrt{x^2 + y^2}. \tag{42}$$

The d- and q-axis currents i_d and i_q are regulated by proportional–integral controllers. Fig. 14 shows the picture of the experimental platform. A load geared machine (Fuji
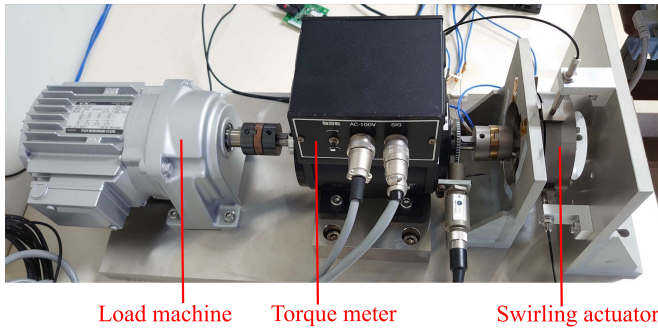
FIGURE 14. Picture of the experimental platform.
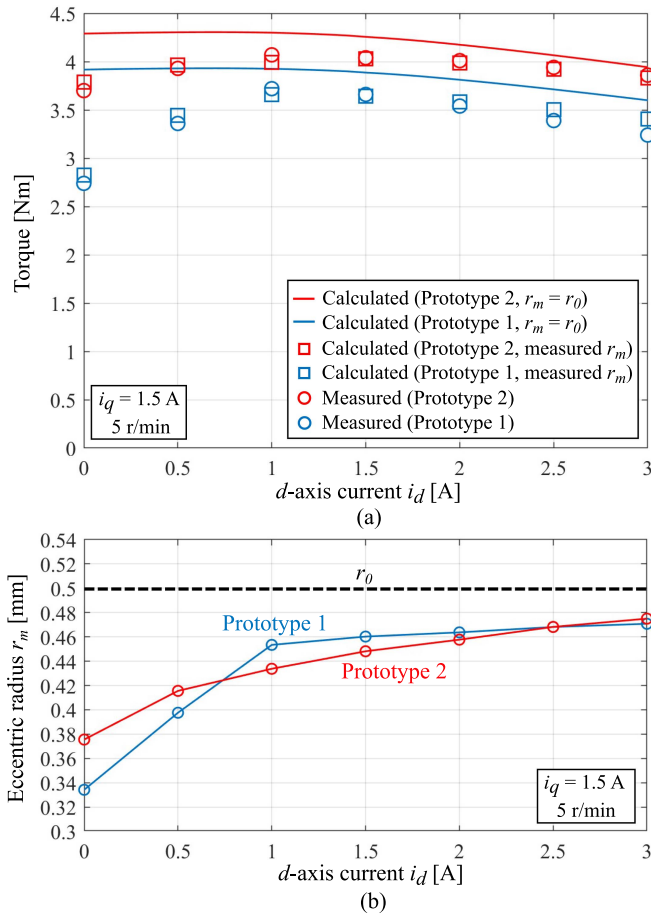
FIGURE 15. (a) Calculated and measured torques and (b) eccentric radius r_m with respect to the d-axis current i_d.

Hensokuki VX02-025M) with the rated speed and torque of 60 r/min and 30 Nm is connected to the swirling actuator shaft through a torque meter (Onosokki SS100). The rotor angular speed ω_r is regulated by the load machine. Moreover, the same lubrication grease is applied on Gear 1 and Gear 2.

Fig. 15 shows the calculated torque, measured torque, and measured eccentric radius r_m with respect to the d-axis current i_d. The q-axis current is 1.5 A and the rotor speed is 5 r/min. The coefficient of friction μ is assumed to be 0.4, and the FEA results of F_q are used for the calculation. It is noted
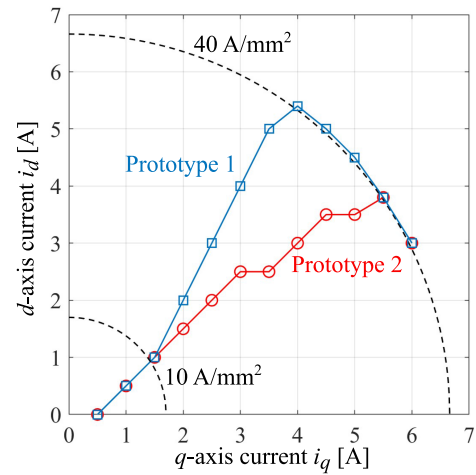
FIGURE 16. Current operation points at the rotor speed of 5 r/min.

that r_m increases as i_d increases, indicating that increasing the d-axis force F_d can enlarge r_m. The torque calculated by assuming $r_m = r_0$ has a large discrepancy compared with the measured torque due to the discrepancy between r_m and r_0. If the measured value of r_m is used for the calculation, the discrepancy becomes small. Prototype 2 has a higher torque than that of prototype 1.

Fig. 16 shows the current operation points of prototype 1 and prototype 2 at the rotor speed of 5 r/min. For each value of i_q, i_d that generates the maximum torque is selected. The current amplitude is limited by the peak current density of 40 A/mm^2. It is shown that the required i_d increases as i_q increases. Prototype 1 suffers from the insufficient i_d when i_q exceeds 3.5 A. In contrast, Prototype 2 needs less i_d to generate the maximum torque. This indicates that the smaller pressure angle α of Gear 2 reduces the required F_d. As a result, the required i_d is reduced.

Fig. 17 shows the calculated torque, measured torque, and measured eccentric radius r_m with respect to the q-axis current i_q. The measured torque of the previous prototype in [22] is also shown for comparison. It is noted that r_m decreases as the torque increases. There is an obvious decrease of r_m in prototype 1 when i_q exceeds 3.5 A due to the limited i_d as shown in Fig. 16. For both prototype 1 and prototype 2, the calculated torques with the measured r_m agree with the measured torques when i_q is lower than 3 A. When i_q is larger, there are discrepancies between the calculated and measured torques. The possible reason is that μ is not constant and increases with the torque. The peak measured torques of prototype 1 and prototype 2 are 7.4 and 10.0 Nm, respectively. The corresponding peak torque densities are 47 and 64 Nm/L, which are significantly improved compared with the peak torque density of 27 Nm/L of the previous prototype in [22].

C. LOSS AND THERMAL EVALUATIONS

To evaluate the power and losses of the prototypes, a digital power analyzer (Yokogawa WT1803E) is used to measure the input electric power P_{in} and currents. The output power P_r is
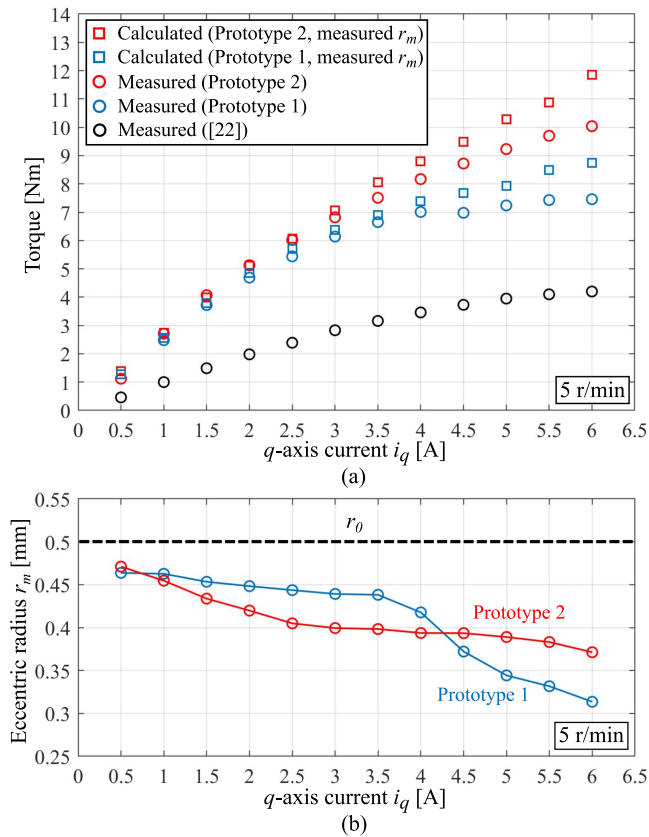
FIGURE 17. (a) Calculated and measured torques and (b) measured eccentric radius r_m with respect to the q-axis current i_q.
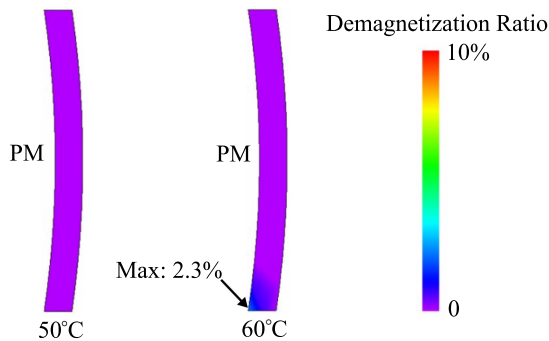
FIGURE 18. FEA results of the irreversible demagnetization ratio of the PM at 40 A/mm².

calculated by the measured rotor speed and torque from the torque meter. Then, the actuator efficiency is given by

$$\eta_s = \frac{P_r}{P_{\text{in}}}. \qquad (43)$$

The losses consist of copper, iron, and mechanical losses. The iron loss is obtained by 3-D FEA, which is dominantly due to the eddy current loss in the swirler iron core that is not laminated but solid instead.

Table 2 lists the powers and losses of the two prototypes at 5 and 30 r/min. The currents are $i_d = 1$ A and $i_q = 1.5$ A, corresponding to the rated current density of 10 A/mm². The

TABLE 2. Powers and Losses at Rated Current Density ($i_d = 1$ A, $i_q = 1.5$ A)

	Prototype 1		Prototype 2	
Rotor speed [r/min]	5	30	5	30
Current frequency [Hz]	9.4	56.5	12.5	75
Torque [Nm]	3.6	3.0	4.1	3.5
Input power [W]	24.3	35.1	24.7	39.0
Output power [W]	1.9	9.4	2.2	11.0
Copper loss [W]	20.8	20.8	20.8	20.8
Iron loss [W]	0.1	1.6	0.1	2.6
Mechanical loss [W]	1.4	3.3	1.6	4.6
Actuator efficiency	7.8%	26.8%	8.9%	28.2%

TABLE 3. Measured Temperatures of Windings and PMs

Current density [A/mm²]	10	20	40
Operation time [s]	1800	60	10
Maximum winding temperature [°C]	70.8	74.1	76.5
Maximum PM temperature [°C]	45.1	34.5	36.3

copper loss is dominant since the maximum speed of the prototypes is as low as 30 r/min. When the rotor speed increases, the torque decreases and the mechanical and iron losses increase. Due to the higher transmission ratio, prototype 2 has a higher current frequency at the same rotor speed. Thus, the iron loss of prototype 2 is slightly higher. At 30 r/min and 10 A/mm², the actuator efficiencies of the two prototypes are 26.8% and 28.2%, respectively.

The thermal characteristics are investigated by measuring the winding and PM temperatures using thermocouples. Table 3 lists the measured temperatures at 10, 20, and 40 A/mm². It is noteworthy that the prototype is air-cooled with a room temperature of 20 °C. After a 30-min operation at the rated current density of 10 A/mm², the winding and PM temperatures reach the steady-state values of 70.8 °C and 45.1 °C, respectively. When the prototype is overloaded at 20 A/mm² for 1 min, the maximum winding and PM temperatures are 74.1 °C and 34.5 °C, respectively. Furthermore, the maximum winding and PM temperatures are 76.5 °C and 36.3 °C, respectively, after an operation of 10 s at the peak current density of 40 A/mm². The temperature limit of the AIW copper wires is 220 °C, which is high enough for the aforementioned operation conditions. Meanwhile, the temperature limit of the PMs depends on the demagnetization condition. In the two prototypes, the PMs are made of N48H and have a thickness of 1 mm. Fig. 18 shows the FEA results of the irreversible demagnetization ratio on the PM at the current density of 40 A/mm². The demagnetization ratio is defined as the amount of variation in the residual flux density of the PM. The irreversible demagnetization occurs around one corner of the PM when the PM temperature is 60 °C. The operating conditions shown in Table 3 are permissible since the PM temperatures
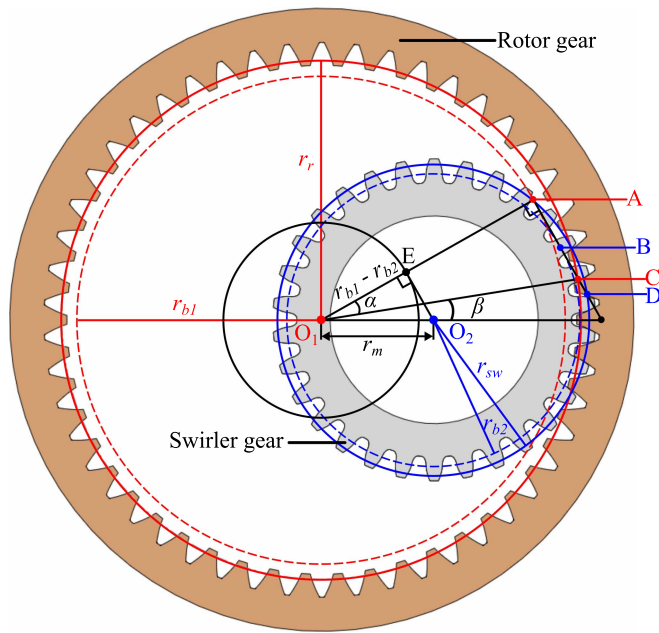
FIGURE 19. Schematic for calculating the gear center distance r_m.

do not go beyond 60 °C. However, if the actuator needs to be periodically overloaded, the overloaded operation time should be limited.

VI. CONCLUSION

This article presented the torque density improvement of the swirling actuator, which is driven by the electromagnetic radial force and high-transmission-ratio mechanical gears. By reducing the nominal air-gap length and PM thickness, the active electromagnetic radial force was enhanced by 86% compared with the previous model. An improved gear design with a higher transmission ratio of 150 and a reduced pressure angel of 20° was also designed. Two prototypes were built and the torques, losses, and thermal characteristics were investigated. It was shown that the reduced pressure angle helped decrease the required d-axis current. The peak torque density was improved from 27 to 47 Nm/L with the enhanced electromagnetic radial force and was further improved to 64 Nm/L with the improved gear design.

APPENDIX

Fig. 19 shows the schematic for calculating the gear center distance r_m. Point O_1 and O_2 are the centers of the rotor gear and swirler gear, respectively. The red and blue solid circles are the base circles of the rotor gear and swirler gear with the radii of r_r and r_{sw}, respectively. The red and blue dashed circles are the base circles of the rotor gear and swirler gear with the radii of r_{b1} and r_{b2}, respectively. The r_{b1} and r_{b2} satisfy the following equations:

$$r_{b1} = r_r \cos\alpha, r_{b2} = r_{sw} \cos\alpha. \tag{44}$$

The segment AD is the common tangent of the two base circles. Let us draw an auxiliary circle that is concentric with

the rotor gear and has a radius of $(r_{b1} - r_{b2})$. The segment O_2E is the tangent of the auxiliary circle and is parallel with the segment AD. Thus,

$$r_m = \frac{r_{b1} - r_{b2}}{\cos(\alpha + \beta)}. \tag{45}$$

Moreover, the pitch circle radii are given by

$$r_r = \frac{Z_r m}{2}, r_{sw} = \frac{Z_{sw} m}{2}. \tag{46}$$

By substituting (44) and (46) into (45), r_m is derived as

$$r_m = \frac{(Z_r - Z_{sw})}{2} \frac{\cos\alpha}{\cos(\alpha + \beta)} m. \tag{47}$$

REFERENCES

[1] A. Penzkofer, G. Cooke, M. Odavic, and K. Atallah, "Coil excited Pseudo direct drive electrical machines," *IEEE Trans. Magn.*, vol. 53, no. 1, Jan. 2017, Art. no. 8200111, doi: 10.1109/TMAG.2016.2603966.

[2] "Pseudo direct drive traction motor," Magnomatics Ltd., 2021. Accessed: Jul. 3, 2022. [Online]. Available: https://www.magnomatics.com/pdd-traction-motor

[3] "HC10DTP," Yaskawa America, 2022. Accessed: Jul. 3, 2022. [Online]. Available: https://www.motoman.com/en-us/products/robots/collaborative/hc-series/hc10dtp

[4] H. Matsuki, K. Nagano, and Y. Fujimoto, "Bilateral drive Gear—A highly backdrivable reduction gearbox for robotic actuators," *IEEE/ASME Trans. Mechatron.*, vol. 24, no. 6, pp. 2661–2673, Dec. 2019, doi: 10.1109/TMECH.2019.2946403.

[5] "RV-N," Nabtesco Corporation, 2022. Accessed: Jul. 3, 2022. [Online]. Available: https://precision.nabtesco.com/en/products/detail/RV-N

[6] "FHA-Mini rotary actuator," Harmonic Drive LLC, 2022. Accessed: Jul. 3, 2022. [Online]. Available: https://www.harmonicdrive.net/products/rotary-actuators/actuators-hollow-shaft/fha-mini

[7] "EC flat," Maxon, 2022. Accessed: Nov. 10, 2022. [Online]. Available: https://www.maxongroup.com/maxon/view/product/607950

[8] "External rotor motors–DFA90," Nanotec Electronic GmbH & Co KG, 2022. Accessed: Nov. 10, 2022. [Online]. Available: https://en.nanotec.com/products/2886-dfa90s024027-a

[9] "μDD motor," MicroTech Laboratory Inc., 2022. Accessed: Nov. 10, 2022. [Online]. Available: https://motor.mtl.co.jp/english/en_products.html

[10] J. Liang, A. Parsapour, E. Cosoroaba, M. Wu, I. Boldea, and B. Fahimi, "A high torque density outer rotor claw pole stator permanent magnet synchronous motor," in *Proc. IEEE Transp. Electrific. Conf. Expo*, 2018, pp. 389–393, doi: 10.1109/ITEC.2018.8450106.

[11] H. Yang et al., "Flux-concentrated external-rotor switched flux memory machines for direct-drive applications," *IEEE Trans. Appl. Supercond.*, vol. 26, no. 7, Oct. 2016, Art. no. 0612606, doi: 10.1109/TASC.2016.2600589.

[12] D. Li, R. Qu, and T. A. Lipo, "High-power-factor vernier permanent-magnet machines," *IEEE Trans. Ind. Appl.*, vol. 50, no. 6, pp. 3664–3674, Nov./Dec. 2014, doi: 10.1109/TIA.2014.2315443.

[13] L. Zhou, F. Guo, H. Wang, and B. Wang, "High-torque direct-drive machine with combined axial- and radial-flux out-runner vernier permanent magnet motor," in *Proc. IEEE Int. Elect. Mach. Drives Conf.*, 2021, pp. 1–8, doi: 10.1109/IEMDC47953.2021.9449499.

[14] Y. Wang, M. Filippini, N. Bianchi, and P. Alotto, "A review on magnetic gears: Topologies, computational models, and design aspects," *IEEE Trans. Ind. Appl.*, vol. 55, no. 5, pp. 4557–4566, Sep./Oct. 2019, doi: 10.1109/TIA.2019.2916765.

[15] M. C. Gardner, M. Johnson, and H. A. Toliyat, "Comparison of surface permanent magnet coaxial and cycloidal radial flux magnetic gears," in *Proc. IEEE Energy Convers. Congr. Expo.*, 2018, pp. 5005–5012, doi: 10.1109/ECCE.2018.8558234.

[16] G. Cooke, R.-S. Dragan, R. Barrett, D. J. Powell, S. Graham, and K. Atallah, "Magnetically geared propulsion motor for subsea remote operated vehicle," *IEEE Trans. Magn.*, vol. 58, no. 2, Feb. 2022, Art. no. 8201005, doi: 10.1109/TMAG.2021.3082999.

[17] L. Jing, W. Tang, T. Wang, T. Ben, and R. Qu, "Performance analysis of magnetically geared permanent magnet brushless motor for hybrid electric vehicles," *IEEE Trans. Transp. Electrific.*, vol. 8, no. 2, pp. 2874–2883, Jun. 2022, doi: 10.1109/TTE.2022.3151681.

[18] K. Atallah, J. Rens, S. Mezani, and D. Howe, "A novel 'Pseudo' direct-drive brushless permanent magnet machine," *IEEE Trans. Magn.*, vol. 44, no. 11, pp. 4349–4352, Nov. 2008, doi: 10.1109/TMAG.2008.2001509.

[19] Q. Wang, S. Niu, and S. Yang, "Design optimization and comparative study of novel magnetic-geared permanent magnet machines," *IEEE Trans. Magn.*, vol. 53, no. 6, Jun. 2017, Art. no. 8104204, doi: 10.1109/TMAG.2017.2662947.

[20] S. Yousefnejad, H. Heydari, K. Akatsu, and J.-S. Ro, "Analysis and design of novel structured high torque density magnetic-geared permanent magnet machine," *IEEE Access*, vol. 9, pp. 64574–64586, 2021, doi: 10.1109/ACCESS.2021.3076260.

[21] M. B. Kouhshahi et al., "An axial flux focusing magnetically geared generator for low input speed applications," *IEEE Trans. Ind. Appl.*, vol. 56, no. 1, pp. 138–147, Jan./Feb. 2020, doi: 10.1109/TIA.2019.2946120.

[22] L. Chen, A. Thabuis, Y. Fujii, A. Chiba, M. Nagano, and K. Nakamura, "Principle and analysis of radial-force-based swirling actuator for low-speed high-torque applications," *IEEE Trans. Ind. Appl.*, vol. 58, no. 2, pp. 1963–1975, Mar./Apr. 2022, doi: 10.1109/TIA.2022.3142118.

[23] D. Hwang and T. Higuchi, "A planar wobble motor with a XY compliant mechanism driven by shape memory alloy," *IEEE/ASME Trans. Mechatron.*, vol. 21, no. 1, pp. 302–315, Feb. 2016, doi: 10.1109/TMECH.2015.2439046.

[24] Y. Kadota, K. Inoue, K. Uzuka, H. Suenaga, and T. Morita, "Non-contact operation of a miniature cycloid motor by magnetic force," *IEEE/ASME Trans. Mechatron.*, vol. 18, no. 5, pp. 1563–1571, Oct. 2013, doi: 10.1109/TMECH.2012.2208225.

[25] S. O. Schrade et al., "Development of VariLeg, an exoskeleton with variable stiffness actuation: First results and user evaluation from the CYBATHLON 2016," *J. NeuroEng. Rehabil.*, vol. 15, 2018, Art. no. 18, doi: 10.1186/s12984-018-0360-4.

[26] A. Chiba, T. Fukao, O. Ichikawa, M. Oshima, M. Takemoto, and D. G. Dorrell, *Magnetic Bearings and Bearingless Drives*. Amsterdam, The Netherlands: Newnes Elsevier, 2005.

[27] Z. Q. Zhu, D. Ishak, D. Howe, and J. Chen, "Unbalanced magnetic forces in permanent-magnet brushless machines with diametrically asymmetric phase windings," *IEEE Trans. Ind. Appl.*, vol. 43, no. 6, pp. 1544–1553, Nov./Dec. 2007, doi: 10.1109/TIA.2007.908158.

[28] J. Asama, A. Mouri, T. Oiwa, and A. Chiba, "Suspension force investigation for consequent-pole and surface-mounted permanent magnet bearingless motors with concentrated winding," in *Proc. IEEE Int. Elect. Mach. Drives Conf.*, 2015, pp. 780–785, doi: 10.1109/IEMDC.2015.7409148.

[29] D. T. Jelaska, *Gears and Gear Drives*. New York, NY, USA: Wiley, 2012.

LINGYU CHEN (Student Member, IEEE) received the B.E. degree in electrical engineering from the Sichuan University, Chengdu, China, in 2014, and the M.S. degree in power electronics and drives from the South China University of Technology, Guangzhou, China, in 2017. He is currently working toward the Ph.D. degree in electrical and electronic engineering with the Chiba Lab, Department of Electrical and Electronic Engineering, Tokyo Institute of Technology, Tokyo, Japan.

His research interest includes the design and analysis of low-speed high-torque actuators.

YUSUKE FUJII (Member, IEEE) received the B.S., M.S., and Ph.D. degrees in mechanical engineering from the Department of Mechanical Engineering, Shizuoka University, Hamamatsu, Japan, in 2015, 2017, and 2020, respectively.

Since September 2019, he has been a Visiting Scholar with the University of Wisconsin-Madison, Madison, WI, USA, for half a year, where he has been involved in bearingless induction motors. He is currently an Assistant Professor with the Department of Electrical and Electronic Engineering, Tokyo Institute of Technology, Tokyo, Japan. His research interests include bearingless motors, magnetic bearings, and motor drives.

Dr. Fujii is a member of the Institute of Electrical Engineers of Japan and the Japan Society of Mechanical Engineers.
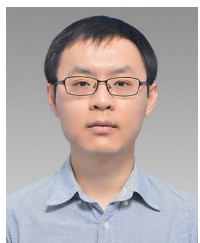
AKIRA CHIBA (Fellow, IEEE) received the B.S., M.S., and Ph.D. degrees in electrical engineering from the Tokyo Institute of Technology, Tokyo, Japan, in 1983, 1985, and 1988, respectively.

In 1988, he joined the Tokyo University of Science, Tokyo, Japan, as a Research Associate with the Department of Electrical Engineering, Faculty of Science and Technology. Since 2010, he has been a Professor with the School of Engineering, Tokyo Institute of Technology, Tokyo, Japan. He has been studying magnetically suspended bearingless ac motors, super high-speed motor drives, and rare-earth-free-motors for automotive traction applications. He has so far authored or coauthored more than 1170 papers including the first book on "Magnetic Bearings and Bearingless Drives" in 2005.

Prof. Chiba was the recipient of the First Prize Paper Award from the Electrical Machine Committee in the IEEE IAS in 2011 on a rare-earth-free motor, the second and third place Best Paper Awards in IEEE TRANSACTIONS ON ENERGY CONVERSION in 2016 and 2017, respectively, the IEEJ Prize Paper Awards in 1998, 2005, 2018, and 2020 Nikola Tesla Award, and one of IEEE Technical Field Awards. He has served as a Secretary, a Vice-Chair, a Vice-Chair-Chair-Elect, a Chair, and a Past-Chair in the Motor Sub-Committee in the IEEE PES during 2007–2016. He was a Member, Chair, and Past-Chair in the IEEE Nikola Tesla Field Award Committee in 2009–2014. He has served as a Chair in IEEE-IAS Japan Chapter in 2010–2011. He was an ECCE Vice-Chair in technical committee during 2016–2019. He was a Technical Co-Chair in IEEE IEMDC 2017 held in Miami, FL, USA. He is TCPRC and was an Associate Editor in IEEE TRANSACTIONS ON INDUSTRY APPLICATIONS since 2020 and from 2011 to 2019, respectively. He was a Founding Chair in the Motor Technical Committee in Japan Society of Automotive Society in 2012–2018. He has served as a Secretary, Vice Chair, Chair, and Past-Chair in IEEE-IAS Electric Machine Committee since 2016. He has been serving as an Editor in IEEE TRANSACTIONS ON ENERGY CONVERSION since 2013. He has served as the IEEE IAS Fellow Committee Executives from 2017 to 2020. He has been the Chair in IEEJ Electric Machine Committee since 2020. He has been serving as an Examiner in the Nagamori Award since 2015. He was the Department Head of Electrical and Electronics Department during 2014 and 2016 and led MOOC project of the introduction of Electrical and Electronics Engineering, released in May 2017 through EDX. He has led active learning with internet Handbook application in undergraduate and graduate course lectures.